Micro-earthquakes beneath Ice Streams B and C, West Antarctica: observations and implications

S. Anandakrishnan

Earth System Science Center and Department of Geosciences, Pennsylvania State University, University Park, Pennsylvania 16802, U.S.A.

C. R. Bentley

Geophysical and Polar Research Center, University of Wisconsin–Madison, Madison, Wisconsin 53706, U.S.A.

ABSTRACT. Micro-earthquakes have been monitored at two locations on Ice Stream B and one on Ice Stream C using a seismographic array built specifically for that purpose. Subglacial micro-earthquakes are 20 times more abundant beneath Ice Stream C than beneath Ice Stream B, despite the 100 times more rapid movement of Ice Stream B. Triangulation shows the foci beneath Ice Stream C, like those beneath Ice Stream B, to be within a few meters of the base of the ice, presumably within the uppermost part of the bed, and fault-plane analysis indicates slips on horizontal planes at about a 30° angle to the presumed direction of formerly active flow. Source parameters, computed from spectra of the arrivals, confirmed that the speed of slip is three orders of magnitude faster beneath Ice Stream C than beneath Ice Stream B which means that a five orders-of-magnitude greater fraction of the velocity of Ice Stream C is contributed by the faulting, although that fraction is still small. We attribute the difference in activity beneath the two ice streams to the loss of dilatancy in the till beneath Ice Stream C in the process that led to its stagnation.

INTRODUCTION

The West Antarctic ice sheet is drained to the Ross Ice Shelf by the so-called "Ross ice streams" on the Siple Coast (Fig. 1). These ice streams, with the striking exception of Ice Stream C, have high surface velocities (400–800 m a^{-1}). Fast-moving (450 m a^{-1}) Ice Stream B has been extensively studied in the past decade; neighboring Ice Stream C, though similar in dimensions, is moving slowly ($\sim$5 m a^{-1}). At one time, Ice Stream C had a velocity presumably comparable to the present velocity of Ice Stream B (Rose, 1979; Shabtaie and Bentley, 1987), probably as recently as 130 years ago (Retzlaff and Bentley, in press). A viable explanation for the high velocity of Ice Stream B has been advanced (Alley and others, 1987a, b; Blankenship and others, 1987b; Rooney and others, 1987; these four papers together are hereafter referred to as Till 1–4); in this paper we suggest an explanation for the low velocity of Ice Stream C.

The authors of Till 1–4 hypothesized that the fast flow of Ice Stream B is due to a thin layer of deforming sediment at its base. The presence of a weak layer beneath the ice stream was deduced from active-source seismic experiments at Upstream B camp (UpB; see Fig. 1), and has since been confirmed by drilling to the base of the ice stream (Engelhardt and others, 1990). This meters-thick layer, because it is highly porous and saturated with water at high pore pressure, has very low shear strength
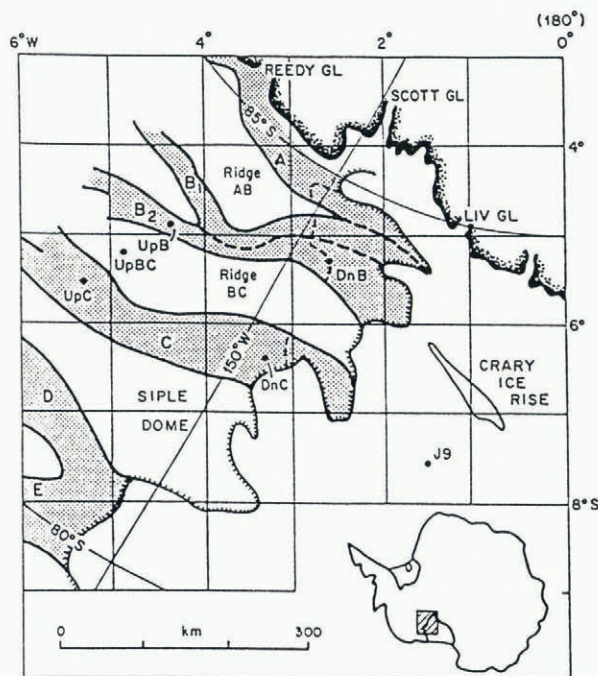

Fig. 1. Location map of the Siple Coast region showing the Ross ice streams (shaded) and UpB and UpC camps (solid circles on Ice Streams B_2 and C, respectively). In the rectangular grid coordinate system shown here, the origin is at the South Pole, grid north is towards Greenwich, and one grid degree equals one degree of geographic latitude. The ice streams flow grid south-eastward into the Ross Ice Shelf.
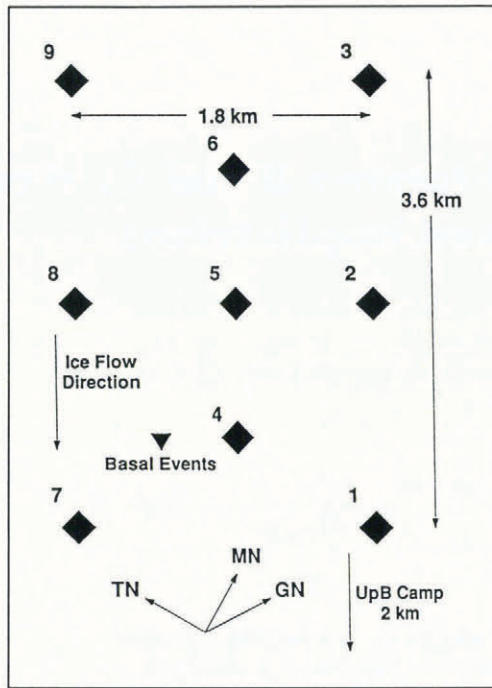
Fig. 2. Sketch map showing the lay-out of the passive seismic array at UpB. TN is true north, MN is magnetic north and GN is grid north. The diamonds mark the locations of the seismometers and the triangle marks the epicenters of the basal micro-earthquakes.
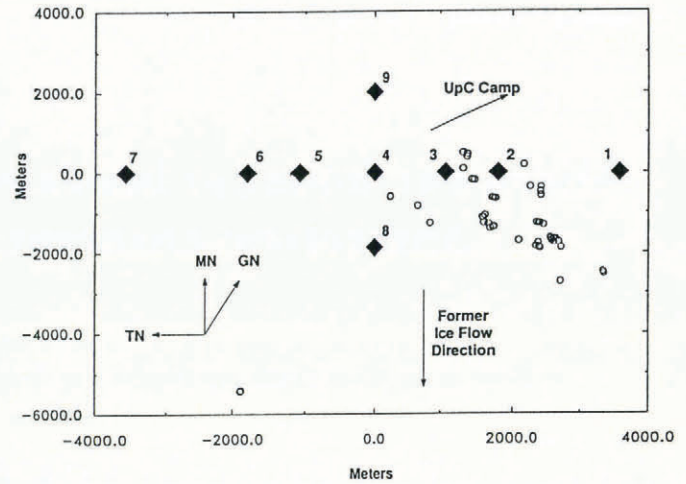

Fig. 3. Sketch map showing the lay-out of the passive array at UpC. TN is true north, MN is magnetic north and GN is grid north. The diamonds mark the locations of the seismometers and the circles the epicenters of the basal micro-earthquakes. The arrow shows the direction to UpC camp, 6 km away.

and is believed to deform readily in response to the shear stress applied by the overlying ice stream. Most of the velocity of Ice Stream B is believed to be taken up in rapid deformation of this till layer (Alley and others, 1987a; Kamb, 1990).

Such a layer presumably played a similar role beneath Ice Stream C when it was moving rapidly. Now, however, to a much greater extent than beneath Ice Stream B, the basal shear stress results in faulting at discrete sites either within this layer or at the ice/sediment interface. A micro-earthquake monitoring network at Upstream C camp (UpC; Fig. 2) on Ice Stream C detected over a hundred basal micro-earthquakes, whereas a similar monitoring network at UpB detected only six basal events in a similar time span. In addition, the UpC events were considerably larger than the UpB events.

EXPERIMENTS

During the 1985–86 Antarctic field season the micro-earthquake monitoring network built at the University of Wisconsin was deployed at UpB (Blankenship and others, 1987a). It was subsequently re-deployed at Downstream B camp (grid 5.2° S, 2.5° W) on the ice plain of Ice Stream B in 1987–88 and at UpC in 1989–90. This "passive seismic" network consisted of nine high-frequency three-component digital seismometers connected by fiber-optic cable to a central computer and recording station. At UpB (Fig. 2), the network was designed primarily to detect events at the base of Ice Stream B and thus a broad spread was deployed both cross-stream and in-stream to ensure good hypocenter solutions. At UpC (Fig. 3), the network was used also as

the recording site for a refraction line 60 km long (Munson and Bentley, in press); the long cross-stream leg allowed accurate determination of apparent velocities of refracted arrivals. The two off-line stations allowed us to determine hypocenters of basal events, but with lower accuracy than at UpB. No basal events were detected at Downstream B, so we do not consider that experiment further here.

Upstream B

The passive seismic network at UpB was active for 85 h over a period of $2\frac{1}{2}$ weeks. A trigger algorithm in the data logger initiated recording of all channels when a micro-earthquake was detected. Station 5 was always used as the trigger station. Twenty-five micro-earthquakes were recorded, including nine that originated at the base of the ice stream (the remainder had near-surface sources, presumably related to crevasses). We discuss only the six basal events that were recorded at all nine stations — the remaining three were too small to pick accurately and analyze. The epicenters of these basal events, all of which appeared to occur on the same fault plane, are marked by the triangle in Figure 2. A fuller discussion of the observational program at UpB has been given by Blankenship and others (1987a). We have added here an analysis of the fault-plane solution, seismic moments (a measure of seismic energy release) and slip.

Upstream C

The network was in place at UpC from 1 December 1988 to 4 January 1989. During this period the system was operated for 110 h. A dual-channel trigger was used for most of the experiment to ensure that the data logger only recorded events large enough to be present at more than one station — small, local events such as firnquakes and cultural noise would not trigger the array. A pre-trigger period of 2 s and a post-trigger period of 3 s were recorded. The sampling interval for all channels was

0.4 ms. The storage medium (Bernoulli 10-Mbyte disks) could hold 15 events. Each seismometer was powered by a 12 V car battery connected to a 20 W solar panel. The central receiving site and data-logging computer were powered by a 1 kW gasoline-powered generator. The generator would run continuously for 24 h, at the end of which time the system was serviced and the data disk changed. Generally, the disk would fill with data before the generator shut down; on rare occasions, the generator failed early and the length of active service is unknown. Figure 4 is a typical seismogram from an event at UpC.
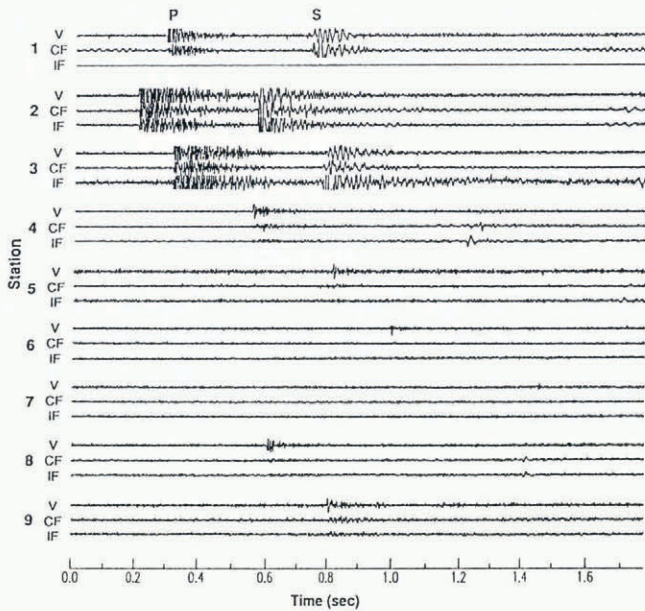

Fig. 4. Seismogram of a typical basal event at UpC. The numbers 1–9 refer to the corresponding three-component remote station. The trace marked V is the vertical component and those marked IF and CF are the inflow (i.e. parallel to the axis of the ice stream) and cross-flow components, respectively. P and S arrivals are marked on the top set of traces. The IF channel at station 1 is dead.

ANALYSIS

The analysis of all events followed the same path. The times of arrival of the P (compressional) waves were picked from the seismogram using an interactive, computer-based seismic analysis program. We used only P-wave arrivals because the P-wave velocity, v_P(ice), is known more accurately than the S-wave velocity. These times, and the corresponding station locations, were inverted to locate the hypocenter using a generalized inverse algorithm. The polarities of the first motions of the P waves were used to determine the "fault-plane solution", i.e. the orientation of the fault plane and the direction of the fault motion. Finally, the spectra of the arrivals were used to determine the moments of the events.

Location

The micro-earthquake location algorithm we used was as outlined in Lee and Stewart (1981). The hypocenter is calculated by minimizing the residual between the observed arrival time at a station and a theoretical arrival time. This procedure was iterated until the error (the sum of the squares of the residuals) converged to a minimum.

The choice of velocity model in the ice stream has an important influence on the accuracy with which hypocenters can be located. To simplify the model, we assumed lateral homogeneity within the bounds of the seismic network. We modeled the ice stream as a set of flat layers, each with a non-negative linear velocity–depth gradient. The zone of greatest velocity gradient is the firn (approximately the top 35 m at UpB and the top 70 m at UpC). This zone was modeled as 12–15 thin (2–10 m thick) individual layers, using v_P in the firn as determined by seismic refraction shooting (Anandakrishnan and others, 1988; Anandakrishnan, 1990). The zone from the bottom of the firn to the base of the ice stream was treated as a constant-velocity layer. Since v_P(ice) decreases with temperature and the refraction shooting determines the velocities only near the top of the ice stream, which is the coldest part of the ice column, we applied a correction to v_P(ice) of -2.3 m s^{-1} K^{-1} (Kohnen, 1974) from the surface temperature of $-25°$C to an ice-column mean temperature of $-18°$C (Shabtaie and others, 1987). It is easy to show that the differences in ray paths and travel times between straight rays in a mean-temperature column and the slightly curved rays in the real ice column are negligible. Finally, receiver-elevation differences, Δz, were taken into account by applying a ray-path-dependent elevation correction, Δt, to the travel time, where $\Delta t = \Delta z \cos \phi / v_P$(ice). In effect, the firn-layer thickness is assumed to be the same beneath all the receivers, so changes in surface elevation result in a shorter or longer path within the constant-velocity ice.

Fault-plane solutions

Next, we calculated the fault planes and moments for each event. The distribution of first motions of the P waves was used to determine the orientation of the fault and the direction of the slip — the fault-plane solution. The amplitudes of the arrivals were corrected for the radiation pattern at the source using the fault-plane solution; we determined the moments from these corrected-amplitude seismograms.

A double-couple model of the source, which we have assumed to apply, separates the focal sphere (a small sphere surrounding the fault) into four quadrants bounded by two orthogonal nodal planes (the fault plane and the auxiliary plane). Each quadrant should exhibit only compressional or dilatational first motion, and should be different from its neighboring quadrants (e.g. Aki and Richards, 1980; Lee and Stewart, 1981). Plotting the polarities of first motions of the arrivals on an equal-area (Schmidt) plot representing the focal sphere should reflect this pattern. Two orthogonal great circles, representing planes, then should separate the compressional from the dilatational arrivals; their positions and the pattern of first motions yield two alternative solutions for the strike, dip and slip directions of the fault. It is the usual practice in teleseismic work to use the lower hemisphere of the focal sphere, but since the rays in our study were up-going, we chose an upper-hemisphere
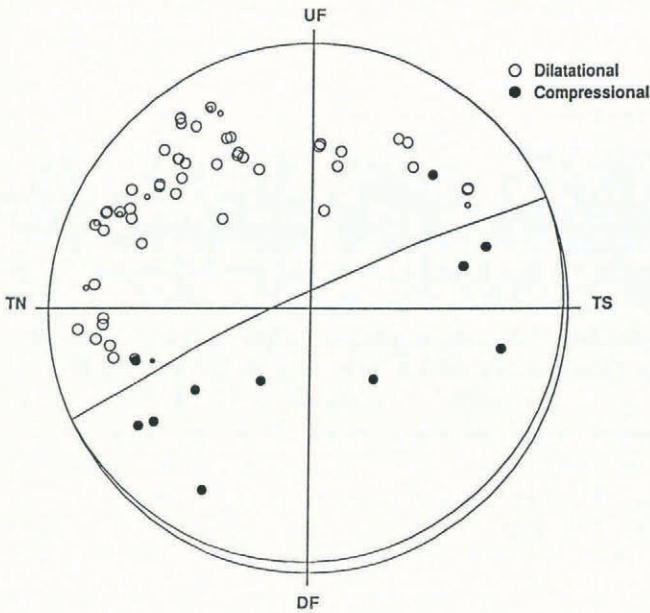
Fig. 5. Schmidt diagram of the upper hemisphere of the focal sphere for one set of micro-earthquakes at Upstream C. Open circles represent dilatational first motions and solid circles represent compressional first motions. Conjugate horizontal diameters of the focal sphere are marked TN and TS for true north and true south and UF and DF for directions approximately upflow and downflow. Because of the very slow speed of Ice Stream C, the direction of movement is not known precisely.

representation instead. The hypocentral location program provided the azimuths and the take-off angles of the rays. Figure 5 is a Schmidt plot of 11 micro-earthquake events that occurred within a period of 20 min at UpC. We have assumed that all these events, which occurred so
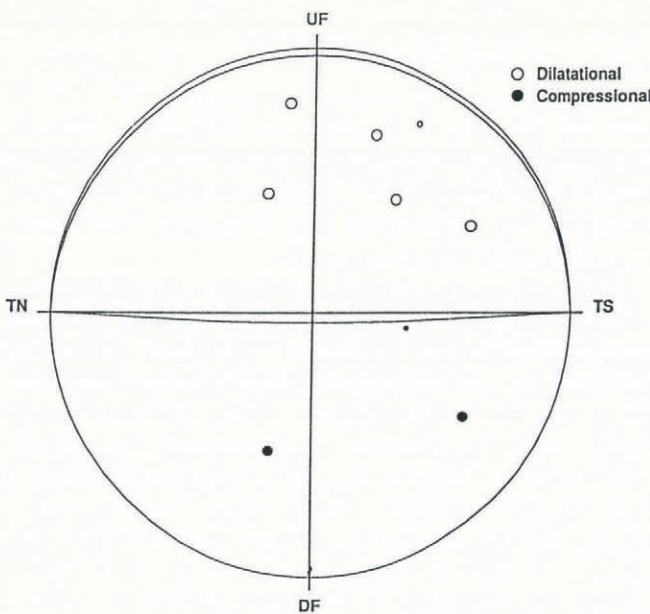

Fig. 6. Schmidt diagram of the upper hemisphere of the focal sphere for the micro-earthquakes at Upstream B. Open circles represent dilatational first motions and solid circles represent compressional first motions. Conjugate horizontal diameters of the focal sphere are marked TN and TS for true north and true south, and UF and DF for directions approximately upflow and downflow.

soon after one another, shared the same fault-plane and we have therefore combined all the arrivals on to one plot. A solution consistent with the events in Figure 5, and all the other events recorded at UpC as well, is a plane dipping 8° ± 5° downstream and a slip direction of 30° ± 20° to left of the ice-stream axis. (The alternative type of solution, namely a fault plane that is nearly vertical, we reject for common-sense reasons.) Due to the low velocity of Ice Stream C, the flow direction at UpC is not well determined and may not be axial. Thus, we cannot tell whether the slip direction deviates from the flow direction.

For UpB, the first-motion diagram (Fig. 6) implies a fault of negligible dip and slip directly along flow, though the fault-plane solution is poorly constrained.

Moments

The seismic moment M_0, a measure of the energy of an earthquake, is defined by

$$M_0 = \mu \bar{u} A \tag{1}$$

where μ is the rigidity and $\bar{u}$ is the average slip over the fault area A. To relate the moment to the observed displacements we use equation 4.88 of Aki and Richards (1980), in which we replace $A\dot{u}$ by an integral of the slip over the fault Σ.

$$\dot{\bar{u}} \to s(t) = \int \int_{\Sigma} \Delta \dot{u}(\xi, t) \, \mathrm{d}\Sigma$$

where ξ is the position of the differential unit of area $\mathrm{d}\Sigma$ and Δu is the slip at that location. Taking the Fourier transform, $S(\omega)$, of $s(t)$ and then setting $\omega = 0$ we have (Aki and Richards, 1980, vol. 2)

$$S(0) = \int \int_{\Sigma} \Delta u(\xi, t \to \infty) \, \mathrm{d}\Sigma = \bar{u}A.$$

Thus, $S(0)$ is the product of total slip $\bar{u}$ and fault area A and $M_0 = \mu S(0)$. The Fourier transform of Aki and Richards' (1980) equation 4.88 is

$$u_{\mathrm{P}}(x, \omega) = \frac{\mathcal{F}^{\mathrm{P}}(\omega)}{4\pi \rho_{\mathrm{s}}^{\frac{1}{2}} \rho_{\mathrm{d}}^{\frac{1}{2}} v_{\mathrm{ps}}^{\frac{5}{2}} v_{\mathrm{pd}}^{\frac{1}{2}} \ell}$$

whence

$$M_0 = \left(\frac{u_{\mathrm{P}}(x, \omega \to 0)\ell}{\mathcal{F}^{\mathrm{P}}} \right) 4\pi \rho_{\mathrm{s}}^{\frac{1}{2}} \rho_{\mathrm{d}}^{\frac{1}{2}} v_{\mathrm{ps}}^{\frac{5}{2}} v_{\mathrm{pd}}^{\frac{1}{2}} \tag{2}$$

where $u_{\mathrm{P}}(x, \omega)$ is the angular-frequency (ω) spectrum of the surface displacement, x has the components, (x, y, z), $\mathcal{F}^{\mathrm{P}}$ is the radiation-pattern correction (a function of fault orientation), ℓ is the distance from source to receiver, and ρ_{s}, v_{ps}, ρ_{d} and v_{pd} are the density and P-wave velocity at the source and at the detector, respectively.

We determine $u_{\mathrm{P}}(x, \omega \to 0)$ by taking the Fourier transform of the P-wave arrival. A 0.4 s Hamming window centered on the P wave was applied prior to the transform. Figure 7 is a plot of the spectrum from one such P-wave arrival. Following Brune (1970), we fit a function of the form

$$\Omega(\omega) = \frac{\Omega(0)}{1 + (\omega/\omega_0)^2} \tag{3}$$

to the data and determine the low-frequency spectral level $u_{\mathrm{P}}(x, \omega \to 0) = \Omega(0)$.
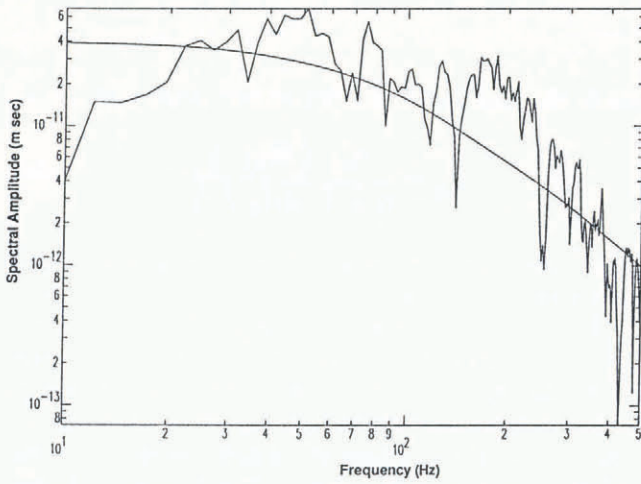
Fig. 7. Plot of P-wave displacement spectrum for one arrival. The smooth curve is the function $\Omega(\omega)$.

RESULTS

The data collected at UpC are summarized in Table 1. During the 110 h of operation, 161 micro-earthquakes were recorded. Selected events were analyzed to

Table 1. Times of recording of micro-earthquakes at UpC. Ending times marked with asterisk are on the day following the start time. The numbers of the station(s) used for triggering are in parentheses in the last column

Date	Start	End	Events	Trigger
	Local time			
year-month -day				
88-12-01	1340	1410	14	Single (3)
88-12-06	1930	2015	15	Single (3)
88-12-08	2130	0050*	14	Single (3)
88-12-14	2200	0820*	13	Dual (3, 5)
88-12-15	0930	1115	13	Dual (3, 5)
88-12-15	1115	1120	4	Single (3)
88-12-31	2300	1000	6	Dual (3, 5)
88-12-31	1315	2015	3	Dual (6, 7)
88-12-31	2230	2000*	4	Dual (6, 7)
89-01-02	2300	0900*	0	Dual (6, 7)
89-01-04	2200	0500*	1	Dual (3, 5)
89-01-05	1700	2015	15	Dual (3, 5)
89-01-06	1515	1600	5	Dual (3, 5)
89-01-06	1600	1630	10	Single (3)
89-01-07	1900	1920	11	Single (3)
89-01-08	2000	0215*	1	Dual (2, 6)
89-01-10	2230	0430*	3	Dual (2, 6)
89-01-11	1600	1900	8	Single (2)
89-01-12	2200	1800*	6	Dual (3, 5)
89-01-13	1900	2000	15	Single (3)

determine hypocentral locations, fault-plane solutions and moments. The selection criterion was that the arrivals from these events be detected and picked at most of the stations (generally eight out of the nine). In particular, they must have been picked at the two off-line stations (stations 8 and 9), since the accuracy of location is strongly reduced by the loss of one of these stations. The epicenters of the selected events are mapped in Figure 3.

The sources of error in the depth to the micro-earthquake foci are the uncertainty in $v_P(\text{ice})$, the arrival-time-pick errors and the station-location errors. The total uncertainty δ was determined by

$$\delta = \sqrt{\delta_c{}^2 + \delta_t{}^2 + \delta_d{}^2} \qquad (4)$$

where δ_c, δ_t and δ_d are the depth uncertainties due to errors in assumed velocity, pick time and station location, given by $\delta_c = h(\delta v/v)$, $\delta_t = (h/\ell)v\delta t$ and $\delta_d = \delta z$, respectively. (There is no significant uncertainty in the horizontal positions, which were measured to better than 0.5 m with a laser range-finder.) The ice thickness is h, $v = v_P(\text{ice})$, δv and δz are the uncertainties in $v_P(\text{ice})$ and the detector elevations, respectively, and δt is the picking error. Numerical values for the UpC experiment are $h = 1100 \pm 20$ m, $\ell \simeq 5$ km, $\delta t = 0.4$ ms, $v_P(\text{ice}) = 3.83$ km s^{-1}, $\delta v = 0.03$ km s^{-1} and $\delta z = 5$ m. Thus, $\delta_c = 9$ m, $\delta_t = 0.3$ m and $\delta = 10$ m, the dominant contribution being from the uncertainty in wave velocity.

Our hypothesis is that the micro-earthquakes occur near the base of the ice stream. To test this hypothesis, we compared the hypocentral depths to the ice thickness determined by radar sounding in this region. No radar lines coincided exactly with the located micro-earthquakes, but a profile was run on the long arm of the seismic array — the "X line" — from station 7 to station 1. The micro-earthquakes that occur within a few hundred meters of the X line are at the base of the ice (within the depth-location error). Other event depths are progressively less the farther the events are from the X line in a direction in which the ice thickness is known to diminish. A few of the events occurred within the boundaries of the radar survey of Jacobel and others (1993); there is generally good agreement between the hypocentral depths of those events and the radar-determined bed.

It cannot be determined with certainty whether the micro-earthquakes occur within the ice, at the interface or within a subglacial layer. We consider it unlikely, though, that they occur within the ice. Faulting within a glacier has rarely been observed. Kamb and LaChapelle (1968) did find faults beneath an icefall at the base of Blue Glacier, but the situation there was extreme: the surface slope was 28° and the bed slope was 22°, steepening to 55° a slight distance downstream. Their observation accords with the studies of Butkovich (1956), who found that rapid loading was necessary to cause the ice to act as an elastic material and fracture. In contrast, the rate of change of stress beneath Ice Stream C is small, so the ice near its base probably acts as a plastic material, particularly as it is at or near the melting point.

The other possibilities both must be considered, and in the next section we calculate correspondingly two sets of focal parameters for the micro-earthquakes, since the

moments are functions of the seismic velocities and the densities at the source (see Equation (2)). Values of these variables in the subglacial layer have not been measured but can be estimated. Seismic refraction experiments at UpC (Munson and Bentley, in press) and an examination of refracted arrivals from the micro-earthquakes (Anandakrishnan, 1990) indicate the presence beneath the ice of a sedimentary layer approximately 100–500 m thick in which the seismic velocities are less than the velocity in ice (Anandakrishnan, 1990). Rooney (1988) found from reflection data that within the sedimentary column beneath Ice Stream B, which is probably similar to that beneath Ice Stream C, $v_P \approx 2$ km s^{-1} and $\rho \approx 2$ Mg m^{-3}; Atre and Bentley (1990) found a similar velocity beneath Ice Stream C. We have adopted those values to calculate moments for intra-sediment micro-earthquakes (Table 2).

If the micro-earthquakes occurred right at the ice-sediment boundary, we do not have well-defined parameters; presumably, the moments will lie between values calculated using the velocities and densities respectively in the sediment and in the ice. We have therefore calculated moments for the latter set of parameters as well as the former to provide an upper bound on moments for foci at the boundary (Table 2).

From the moments, we can determine the amount of motion of Ice Stream C that is due to "stick–slip" faulting. We model the base of the ice stream as a slip-plane separating a stationary substrate from the ice stream. All the observed micro-earthquakes have the same fault-plane solution: a plane parallel to the bottom of the ice and slip at 30° counterclockwise from the axis of the ice stream. Individual micro-earthquakes produce slip on only a small part of this plane but, by summing up all the events, we can estimate the contribution to the velocity of the ice stream.

For a series of n earthquakes of moments M_0^1, $M_0^2, \ldots, M_0^n$ occurring in a time interval T and distributed evenly on a slip-plane of area A_b, the average relative velocity of one side of the plane relative to the other (in "stick–slip" motion), v_{ss} is (see Equation (1))

$$v_{ss} = \frac{1}{\mu A_b T} \sum_{i=1}^{n} M_0^i. \qquad (5)$$

Since $\sum_{i=1}^{n} \tau_i$, where τ_i is the inter-event time between events M_0^i and M_0^{i+1}, we can simplify Equation (5) to

$$v_{ss} = \frac{n}{n-1} \frac{\langle M_0 \rangle}{\mu A_b} \frac{1}{\langle \tau \rangle} \qquad (6)$$

where $\langle M_0 \rangle$ is the mean seismic moment and $\langle \tau \rangle$ is the mean inter-event time.

A_b is the area of the bed to which the seismic array was sensitive for an average-sized event, which is different for the two modes in which the array was operated — single-channel and dual-channel trigger. A single-station trigger is sensitive to a part of the bed determined by the radiation pattern of the source. The P-wave radiation pattern for a horizontal double couple is proportional to $\sin 2\phi \cos \theta$ (Aki and Richards, 1980), where ϕ is the take-off angle and θ is the azimuth relative to the slip direction. The displacement at the surface is then proportional to $\sin 2\phi \cos \theta/\ell$. The peak displacement is at $\phi = \pm\pi/4$ and $\theta = 0, \pi$. Call the recorded displacement (in terms of amplifier output voltage) due to an average-size event recorded by the array a and the trigger threshold a_{th}. Then

$$\frac{a_{th}}{a} = \frac{\sin 2\phi \cos \theta/(h/\cos\phi)}{1/(h/\cos\pi/4)}$$
$$= \sqrt{2}\sin 2\phi \cos \theta \cos \phi \qquad (7)$$

determines the (ϕ, θ) region to which the trigger station was sensitive.

Equation (7) defines two approximately elliptical regions of the base of the ice stream (Fig. 8). For the single-station trigger at UpC ($u_P(x, \omega \to 0) = 4.6 \times 10^{-11}$ m s) $a = 0.58$ V and $a_{th} = 0.12$ V; the total area of the two resulting ellipses is 11.3 km^2. The area of sensitivity for a dual-station trigger is determined by setting $a = 1.2$ V (the displacement due to a typical dual-station-trigger event) in Equation (7); a_{th} is unchanged. The intersections of the pairs of regions thus delineated (Fig. 8) have areas of approximately 9 km^2.

Table 2. *Mean seismic moments, $\langle M_0 \rangle$, mean inter-event times, $\langle \tau \rangle$, slip-plane areas, A_b, and stick–slip velocities, v_{ss}, for faults beneath ice streams*

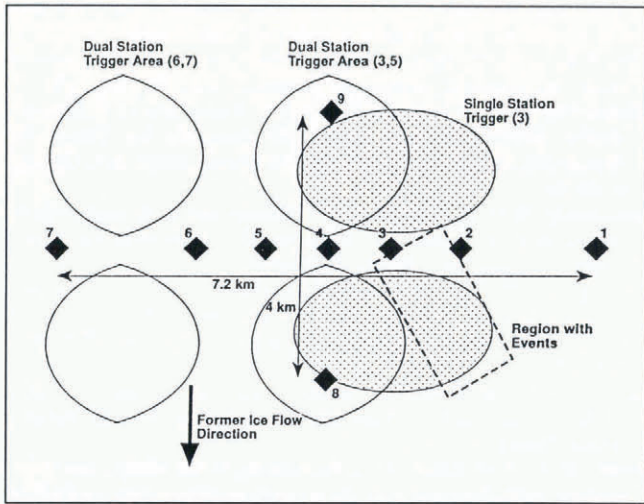| Site	Hypocenter assumed in	Trigger	$\langle M_0 \rangle$	$\langle \tau \rangle$	A_b	v_{ss}
			$\times 10^6$ N m	s	km^2	μm a^{-1}
UpC	Sediment	Single	3.3	136	11.3	33
UpC	Sediment	Dual	5.2	2444	9.4	4
UpC	Ice	Single	14.5	136	11.3	87
UpC	Ice	Dual	23.3	2444	9.4	10
UpB	Sediment	Single	0.8	5×10^4	11.3	0.012
UpB	Ice	Single	2.0	5×10^4	11.3	0.032

Fig. 8. Areas on the bed to which various triggers would be sensitive for a micro-earthquake of average size. The shaded oval is the area for station 3; the unshaded ovals are for the indicated dual-station triggers. The rectangle is the region that contains the micro-earthquakes.

Most of the events recorded occurred in the area marked by the dashed rectangle. Clearly, we would expect a much higher frequency of triggering when station 3 was used as a trigger than for either dual-trigger arrangement. This is reflected in Table 1 — the frequency of events is $13\,h^{-1}$ for "Single (3)", but only $1\,h^{-1}$ or less for the dual triggers — and also in Table 2, which shows v_{ss} for the single-station trigger case to be an order of magnitude greater than for a dual trigger. As the local ice velocity shows no major change in this part of Ice Stream C (Whillans and Van der Veen, 1993), we conclude that the localization reflects a zone of weakness within the bed.

The rigidity $\mu = \rho v_s{}^2$, where v_s is the shear-wave velocity at the source. In ice $v_s = 1.94\,km\,s^{-1}$ and $\rho = 0.917\,Mg\,m^{-3}$, so $\mu = 3.46 \times 10^9\,N\,m^{-2}$. In the bed we assume $v_s = 1\,km\,s^{-1}$ and $\rho = 2\,Mg\,m^{-3}$ (rough estimates since we have no measurements), whence $\mu = 2 \times 10^9\,N\,m^{-2}$.

We used 8 Hz geophones that have a flat response to 250 Hz. The recording system was calibrated and measured prior to deployment so that all channels had identical amplification (see Blankenship and others (1987a) for a description of the recording system). The ambient noise level (the r.m.s. signal in the absence of an event) drifted less than 10% during the course of the season, and some of that change was due to better coupling of the geophones by compaction of the firn.

For events in the sediment, the amplitude-transmission factor $P'P'$ for P waves passing into the ice is $1.05 < P'P' < 1.42$ for the angles of incidence we observe: for the mean angle of incidence $\langle\phi\rangle = 63°$ $P'P' = 1.3$. We have applied this factor to calculate $\langle M_0 \rangle$ for events assumed to be in the sediment.

The mean inter-event times $\langle \tau \rangle$ were determined at UpC simply by taking the mean of the inter-event times between successive events that were successfully located. At UpB, the six events all occurred in a single swarm and no other basal events were observed. Thus, we can only estimate an effective inter-event time at UpB by taking

the total recording time $(T = 85\,h)$ divided by the number of events: $\langle \tau \rangle = T/n = 5 \times 10^4\,s$. (The actual inter-event time between the six events at UpB is $240 \pm 90\,s$, but this obviously is not the value to use in the calculation of v_{ss}.)

The parameters and resulting v_{ss} for faults assumed in the subglacial sediment and in the ice (the upper bound for faulting at the boundary), respectively, for Ice Stream C are summarized in Table 2. Overall, $4\,\mu m\,a^{-1} < v_{ss} < 100\,\mu m\,a^{-1}$, which is four to six orders of magnitude less than the surface velocity of a few $m\,a^{-1}$ measured by I. M. Whillans (personal communication, 1992) for the central part of the ice stream. While small, this speed is three orders of magnitude larger, and the relative contribution to glacial motion some five orders of magnitude larger than beneath Ice Stream B, where slip on faults is responsible for only $0.01-0.03\,\mu m\,a^{-1}$ (Table 2), whereas the surface velocity is $450\,m\,a^{-1}$ (Whillans and others, 1987).

DISCUSSION

Beneath Ice Stream B there is a thin (6–15 m) till layer characterized by a very low effective pressure ($\sim 0.1\,MPa$) and a relatively high porosity ($n \approx 0.4$) that deforms in response to the shear stress at the base of the ice, thus accommodating a high sliding velocity (Till 1–4; Engelhardt and others, 1990). Since rapid deformation of the till must result in transport and discharge of material at the grounding line, either erosion of the till's substrate or an influx of till beneath the head of the ice stream is required to maintain a steady-state system. Presumably, the former rapid motion of Ice Stream C also required a deforming till layer at the bed.

Our results suggest the possibility that the switch from fast to slow flow of Ice Stream C occurred because the dilatant till layer increased in strength owing to a reduction in porosity so that it no longer deformed in a ductile manner. Wong (1990) and Zhang and others, (1987, 1990) performed laboratory experiments on porous rocks that delineated a boundary between brittle and ductile behavior as a function of effective pressure and porosity. They observed that a decrease in porosity below some threshold resulted in a change from homogeneous deformation to shear localized on discrete slip-planes in response to applied stress. Zhang and others (1990) found that at an effective pressure $\Delta P \approx 50\,MPa$ the boundary occurs at porosity $n \approx 0.2$. At lower effective pressures, the boundary is at higher porosity but is not well known. D. M. Davis (personal communication, 1990) estimated that, for $\Delta P = 0.1\,MPa$, n is in the range 0.3–0.4. Thus, a reasonable consequence of a reduction in porosity from $n = 0.4$ to $n \simeq 0.3$ is an increase in seismic activity in the till.

Such a decrease in porosity, associated with a loss of dilatancy, is a likely way to terminate the rapid motion of the ice stream. Whether or not the weak, dilatant bed is the controling factor on the movement rate of the ice stream, it presumably at least provides lubrication of the ice–bed interface without which the ice stream would stagnate. Retzlaff and Bentley (1993) have shown that the stagnation of most of Ice Stream C took place rapidly, i.e.

within a matter of a very few decades at the most. We agree with Retzlaff and Bentley (in press) that such a rapid stagnation could only have been the result of some kind of re-organization of the basal water system.

Free water exists immediately below Ice Stream B (personal communication from H. Engelhardt, 1992) and is needed to draw off the water produced by basal melting (Alley, 1989). The free-water system presumably could re-adjust itself rapidly, as it does under surging glaciers (Kamb, 1987), whereas any process involving water transmission through the nearly impermeable basal till (the hydraulic conductivity in the till beneath Ice Stream B is on the order of $10^{-8} \mathrm{m\,s^{-1}}$ (personal communication from H. Engelhardt, 1992)) or elimination of the lubricating layer by erosion would surely take longer by orders of magnitude.

CONCLUSION

If our observations are representative, micro-earthquakes occur 20 times more frequently at the base of Ice Stream C than at the base of Ice Stream B and contribute more to the motion of the ice stream by about three orders of magnitude in absolute velocity, which is a five order-of-magnitude larger contribution relative to the ice-stream velocity. This result emphasizes the importance of the basal till to controling ice-stream flow. We presume that micro-earthquakes were much fewer also under Ice Stream C when it was active, and that the activity has increased as a result of a decrease in porosity of the subglacial till. If our presumption is correct, the implication is that the transition of the ice stream from fast to slow flow occurred through dewatering and loss of dilatancy in the lubricating till layer.

ACKNOWLEDGEMENTS

REFERENCES

Aki, K. and P. G. Richards. 1980. *Quantitative seismology. Theory and methods.* New York, W.H. Freeman and Co.

Alley, R. B. 1989. Water-pressure coupling of sliding and bed deformation: I. Water system. *J. Glaciol.*, **35**(119), 108–118.

Alley, R. B., D. D. Blankenship, C. R. Bentley and S. T. Rooney. 1987a. Till beneath Ice Stream B. 3. Till deformation: evidence and implications. *J. Geophys. Res.*, **92**(B9), 8921–8929.

Alley, R. B., D. D. Blankenship, C. R. Bentley and S. T. Rooney. 1987b. Till beneath Ice Stream B. 4. A coupled ice-till flow model. *J. Geophys. Res.*, **92**(B9), 8931–8940.

Anandakrishnan, S. 1990. Microearthquakes as indicators of ice stream basal conditions. (Ph.D. thesis, University of Wisconsin–Madison.)

Anandakrishnan, S., D. D. Blankenship, R. B. Alley and C. R. Bentley.

1988. Density-depth profile determined by seismic-refraction studies: Ice Stream B, West Antarctica. (Abstract.) *Ann. Glaciol.*, **11**, 198.

Atre, S. R. and C. R. Bentley. 1990. Laterally varying basal conditions under Ice Stream C, Antarctica. [Abstract.] *EOS*, **71**(43), 1303.

Blankenship, D. D., S. Anandakrishnan, J. L. Kempf and C. R. Bentley. 1987a. Microearthquakes under and alongside Ice Stream B, Antarctica, detected by a new passive seismic array. *Ann. Glaciol.*, **9**, 30–34.

Blankenship, D. D., C. R. Bentley, S. T. Rooney and R. B. Alley. 1987b. Till beneath Ice Stream B: 1. Properties derived from seismic travel times. *J. Geophys. Res.*, **92**(B9), 8903–8911.

Brune, J. N. 1970. Tectonic stress and the spectra of seismic shear waves from earthquakes. *J. Geophys. Res.*, **75**(26), 4997–5009.

Butkovich, T. R. 1956. Strength studies of high-density snow. *SIPRE Res. Rep.* 18.

Engelhardt, H., N. Humphrey, B. Kamb and M. Fahnestock. 1990. Physical conditions at the base of a fast moving Antarctic ice stream. *Science*, **248**(4951), 57–59.

Jacobel, R. J., A. M. Gades, D. L. Gottschling, S. M. Hodge and D. L. Wright. 1993. Interpretation of radar-detected internal layer folding in West Antarctic ice streams. *J. Glaciol.*, **39**(133), 528–537.

Kamb, B. 1987. Glacier surge mechanism based on linked cavity configuration of the basal water conduit system. *J. Geophys. Res.*, **92**(B9), 9083–9100.

Kamb, B. 1990. Is the Antarctic ice sheet disintegrating? *Eng. Sci.*, **53**(3), 5–13.

Kamb, B. and E. R. LaChapelle. 1968. Flow dynamics and structure in a fast-moving icefall. *EOS*, **49**, 312.

Kohnen, H. 1974. The temperature dependence of seismic waves in ice. *J. Glaciol.*, **13**(67), 144–147.

Lee, W. H. K. and S. W. Stewart. 1981. *Principles and applications of microearthquake networks.* New York, Academic Press.

Munson, C. G. and C. R. Bentley. In press. The crustal structure beneath Ice Stream C and Ridge BC, West Antarctica from a seismic refraction and gravity profile. *In* Yoshida, Y., K. Kaminuma and K. Shiraisi, *eds. Recent progress in Antarctic Earth science.* Tokyo, National Institute of Polar Research.

Retzlaff, R. and C. R. Bentley. 1993. Timing of stagnation of Ice Stream C, West Antarctica, from short-pulse-radar studies of buried surface crevasses. *J. Glaciol.*, **39**(133), 553–561.

Rooney, S. T. 1988. Subglacial geology of Ice Stream B, West Antarctica. (Ph.D. thesis, University of Wisconsin–Madison.)

Rooney, S. T., D. D. Blankenship, R. B. Alley and C. R. Bentley. 1987. Till beneath Ice Stream B: 2. Structure and continuity. *J. Geophys. Res.*, **92**(B9), 8913–8920.

Rose, K. E. 1979. Characteristics of ice flow in Marie Byrd Land, Antarctica. *J. Glaciol.*, **24**(90), 63–75.

Shabtaie, S. and C. R. Bentley. 1987. West Antarctic ice streams draining into the Ross Ice Shelf: configuration and mass balance. *J. Geophys. Res.*, **92**(B2), 1311–1336.

Shabtaie, S., I. M. Whillans and C. R. Bentley. 1987. The morphology of Ice Streams A, B, and C, West Antarctica, and their environs. *J. Geophys. Res.*, **92**(B9), 8865–8883.

Whillans, I. M. and C. J. van der Veen. 1993. Patterns of calculated basal drag on Ice Streams B and C, Antarctica. *J. Glaciol.*, **39**(133), 437–446.

Whillans, I. M., J. Bolzan and S. Shabtaie. 1987. Velocity of Ice Stream B and C, Antarctica. *J. Geophys. Res.*, **92**(B9), 8895–8902.

Whillans, I. M., M. Jackson and Y.-H. Tseng. 1993. Velocity pattern in a transect across Ice Stream B, Antarctica. *J. Glaciol.*, **39**(133), 562–572.

Wong, T.-F. 1990. Mechanical compaction and the brittle-ductile transition in porous sandstones. *In* Knipe, R. J. and E. H. Rutter, *eds. Deformation mechanisms, rheology, and tectonics.* Leeds, Leeds University. Department of Earth Sciences, 111–122. (Geological Society Special Publications 54.)

Zhang, J., T.-F. Wong and D. M. Davis. 1987. Failure modes as a function of porosity and effective pressure in porous sandstone. *Geol. Soc. Am. Abstr. Progs.*, **19**, 904.

Zhang, J., T.-F. Wong and D. M. Davis. 1990. Micromechanics of pressure-induced grain crushing in porous rock. *J. Geophys. Res.*, **95**(B1), 341–352.

The accuracy of references in the text and in this list is the responsibility of the authors, to whom queries should be addressed.